



# Prediction of tensile strength and assessing the influence of process parameters of magnetically impelled arc butt welded AISI 409 ferritic stainless steel tubes

Thiyagarajan Muthu Krishnan<sup>1</sup> · Isaac Dinaharan<sup>2</sup> · Ramaswamy Palanivel<sup>3</sup> · Chinnasamy Balamurugan<sup>4</sup>

Received: 26 February 2021 / Accepted: 17 August 2021 / Published online: 6 September 2021  
© The Author(s), under exclusive licence to Springer-Verlag London Ltd., part of Springer Nature 2021

## Abstract

Magnetically impelled arc butt (MIAB) welding is the modern version of the ancient forge welding. The abutting edges are preheated by a rotating arc and upset subsequently. This research work is focused on joining 4-mm thick AISI 409 ferritic stainless steel (FSS) tubes using MIAB welding. Three process parameters namely arc rotation current, upset current, and arc rotation time were varied during welding at five levels according to the chosen central composite design (CCD) of experiments. An empirical relationship was developed to predict the effect of process parameters on the joint strength. The macrostructure and microstructure observations were used to comprehend the predicted plots. Weld zone was composed of fine-grained and deformed structure due to the application of heat and pressure and called as thermo mechanically affected zone (TMAZ). Factors such as poorly forged structure, voids, and oxide particles influenced the joint strength adversely. In spite of significant strengthening of the TMAZ, a clearly forged interface was essential to obtain higher joint strength.

**Keywords** Ferritic stainless steel · Tube · Magnetically impelled arc butt welding · Microstructure · Tensile strength

## 1 Introduction

Ferritic stainless steel (FSS) microstructure is substantially occupied by ferritic phase which imparts body cubic centered (BCC)

crystalline structure. The performance of FSS under the influence of a corrosive environment is analogous to austenitic stainless steels (ASS) due to the alloying element chromium. FSS is economical to ASS because the costlier alloying element nickel is seldom used in the production of this steel. FSS has desirable properties including resistance to stress-induced cracking during corrosion, ability to resist oxidation at elevated temperature, and adequate formability to make appliances in various shapes. Therefore, FSS is preferred to make numerous components in industries especially in automotive sectors and chemical processing plants. Furthermore, FSS is abundantly utilized for domestic applications such as utensil making and electrical items [1–4].

FSS can be readily joined using existing traditional fusion welding methods. Toughness of the joints was found to be compromised. Undue coarsening of grains occurs in the heat-affected zone (HAZ) that affects joint strength. Thermal cycle during fusion welding provides adequate time to form unwanted intermetallic compounds that reduce the resistance to corrosion [5–8]. Joining of tubes necessitates the design of additional fixtures for holding. Solid-state welding can suppress undesirable microstructural features. Friction welding is useful to join tubes but internal flash removal is challenging apart from rigid machine requirement [9]. Friction stir welding (FSW) is another option but the tool is expensive and undergoes rapid wear [10].

---

✉ Thiyagarajan Muthu Krishnan  
muthu.krish07@gmail.com

Isaac Dinaharan  
dinaweld2009@gmail.com

Ramaswamy Palanivel  
rpalanivelme@gmail.com

Chinnasamy Balamurugan  
balamurugan.c@annauniv.edu

- <sup>1</sup> Department of Mechanical Engineering, SRM Valliammai Engineering College, Kattankulathur, Tamil Nadu 603203, India
- <sup>2</sup> Department of Mechanical Engineering Science, University of Johannesburg, Auckland Park Kingsway Campus, Johannesburg, Gauteng 2006, South Africa
- <sup>3</sup> Department of Mechanical Engineering, Shaqra University, Dawadmi, Riyadh 11911, Saudi Arabia
- <sup>4</sup> Department of Mechanical Engineering, College of Engineering, Guindy, Anna University, Chennai, Tamil Nadu 600025, India

**Table 1** MIAB welding window of chosen parameters

No	Parameter	Notation	Unit	Levels				
				-1.682	-1	0	1	1.682
1	Arc rotation current	A	amps	458	475	500	525	542
2	Upset current	U	amps	732	800	900	1000	1068
3	Arc rotation time	T	s	3.5	4.5	6.0	7.5	8.5

Magnetically impelled arc butt (MIAB) welding is the modern version of the ancient forge welding. MIAB was conceptualized back in the 1970s and was termed as ROTARC (rotating arc) welding [11]. The yield strength of the abutting edge region is brought down by electric arc heating to be able to forge. Tubes are fixed to match each other in a straight line and an arc is established by keeping a gap between them. The arc runs along the annular space at high speed under the influence of a magnetic field. The interaction occurring between the arc and the magnetic field was reported to be complex to comprehend. The heating period is determined until the emergence of a molten layer that reduces the stability of the rotating arc. A mechanical force is applied by means of hydraulic or pneumatic arrangement at this stage to accomplish forging of the heated edges. Forging action expels the little molten material to form a flash and creates a solid-state joint. The joint line does not have any solidified material and it is usually denoted as thermo mechanically affected zone (TMAZ). Coarsening of grains does not occur adjacent to the joint line that avoids the formation of vulnerable heat-affected zone (HAZ). No filler metal or shielding gas is used during the process. The size of the flash and metal loss is lower compared to friction welding and flash butt welding [12–15].

Iordachescu et al. [16] analyzed each stage of the MIAB welding process using sequence of photographs and presented the microstructure of ST37 steel joints. Vendan et al. [17] stated that arc current had a remarkable influence on the size of weld zone and depth of penetration in T11 tube weldments. Vendan et al. [18] observed significant strengthening of the joint region in T11 tubular joints. Vendan et al. [19] found that the undesirable impurities were expelled during upsetting and inclusions were avoided in T11 steel joints. Sivasankari et al. [20] observed several phase transformations in the joint region of T11 steel tubes which caused an increase in hardness. Vignesh et al. [21] suggested that computer tomography is a reliable nondestructive method to find out the defect in MIAB welded T11 steel joints. Panda et al. [22] applied a numerical-based evolution approach to develop a functional relationship between process parameters and arc speed to join T11 tubes. Balta et al. [23] compared friction welding and MIAB welding to join AISI 1141 tubes and reached a conclusion that MIAB welding is a good alternative to conventional friction welding. Mosayebnezhad and Sedighi [24] predicted the residual stress

of low alloy steel joints and correlated to the values measured using the hole drilling technique. Kustron et al. [25] concluded that the proper parameters for ultrasonic tests of thin-walled joints can be estimated using numerical methods.

Literature survey revealed that the number of investigations carried out to join metallic materials using MIAB welding is very much limited to a few dozen articles. The primary focus was to join piping steels such as T11 and T91. FSS is extensively used in tubular form in a variety of industries. MIAB welding is a good choice to join FSS tubes to reduce production time. No studies were reported in literature to join FSS tubes using MIAB welding process. Understanding the microstructure evolution and the mechanical behavior as influenced by the process parameters is important. Therefore, this research work was focused to apply MIAB welding to join 4-mm thick FSS tubes and examine the role of process parameters on the joint strength. Design of experiments (DOE) was followed as a strategy to reduce the number of joints. An empirical relationship was estimated to calculate the tensile strength according to the selected process parameter range. DOE approach was widely reported as a methodology for welding processes to predict the responses [26–30].

## 2 Research methodology

### 2.1 Choosing the welding parameters

MIAB welding cycles had several welding parameters (Starting current, Arc initiation time, Arc stabilization time, Arc rotation current, Arc rotation time, Upset current, Upset

**Table 2** Fixed welding parameters

Parameter	Unit	Value
Starting current	amps	525
Arc voltage	v	120
Arc initiation time	s	0.7
Arc stabilization time	s	2.5
Upset time	s	0.3
Upset pressure	MPa	120
Initial gap	mm	1

**Table 3** Chemical composition of AISI 409 ferritic stainless steel

Element	C	Si	Mn	P	S	Cr	Ni	Mo	Al	Cu	Co	Fe
wt.%	0.026	0.467	0.74	0.019	0.015	12.65	0.109	0.028	0.004	0.047	0.039	Balance

time, Upset pressure, and Initial gap) to vary which will eventually affect the joint microstructure and strength [16, 17]. Three welding parameters namely arc rotation current (A), upset current (U), and arc rotation time (T) were chosen to vary during the experimentation based on literature survey and welding trials.

## 2.2 Choosing a window for the welding parameters

Each chosen parameter was varied between two limits which were chosen based on few trial welds and the expertise of the welders. No joining occurred in case of lower level of parameter. Very high range of parameters resulted in excessive melting causing destabilization of the arc and imperfect forging. A coding system was followed to code the upper limit as +1.682 and the lower limit as -1.682. Coding facilitates to record the data during experimentation and post processing to develop an empirical relationship for prediction. The coding for intermediate values was obtained using the following equation.

$$X_i = 1.682 [2X - (X_{\max} + X_{\min})] / (X_{\max} - X_{\min}) \quad (1)$$

where  $X_i$  is the required coded value of a variable  $X$ ;  $X$  is any value of the variable from  $X_{\min}$  to  $X_{\max}$ ;  $X_{\min}$  is the lowest level of the variable;  $X_{\max}$  is the highest level of the variable. Table 1 presents the chosen window of each process parameters. The values of rest of the parameters were maintained constant throughout all experiments as provided in Table 2.

## 2.3 Choosing the design of experiments

Central composite rotatable factorial design (CCD) for three factors was chosen for MIAB welding experiments. Each welding parameter had a variation at five levels as per the chosen experimental design. A sum of 20 experiments is required to perform according to CCD applied for varying three parameters. Experiments consisted of the combination of central values of all process parameters (0,0,0) were carried out repeatedly for six times. A complete theory to comprehend this kind of CCD applied for various processes is presented in established textbooks [31, 32].

## 2.4 MIAB Welding of FSS tubes

This research work used a 4-mm thick AISI 409 FSS tubes. The outer diameter and the length were respectively 44 mm and 150 mm. The composition was tested using X-ray fluorescence (XRF) and the percentage of each element is given in Table 3. Figs. 1 and 2 respectively show the schematic of the stages of MIAB welding process and the actual photograph of the experimental facility used. The edges of the tubes were thoroughly cleaned to remove any foreign material adhering to the abutting surface. The order of experiments presented in Table 4 was randomly done to avoid errors. Each experiment was given a code MW01, MW02, etc., which is used in the figure captions for simplicity. A photograph of typical batch of welded tubes is shown in Fig. 3. The heat input was calculated as per the following expression and furnished in Table 4. The heat transfer efficiency was assumed to be 80%.

**Fig. 1** MIAB welding cycle showing a clamping, b arc initiation, c stable arc rotation, and d upsetting

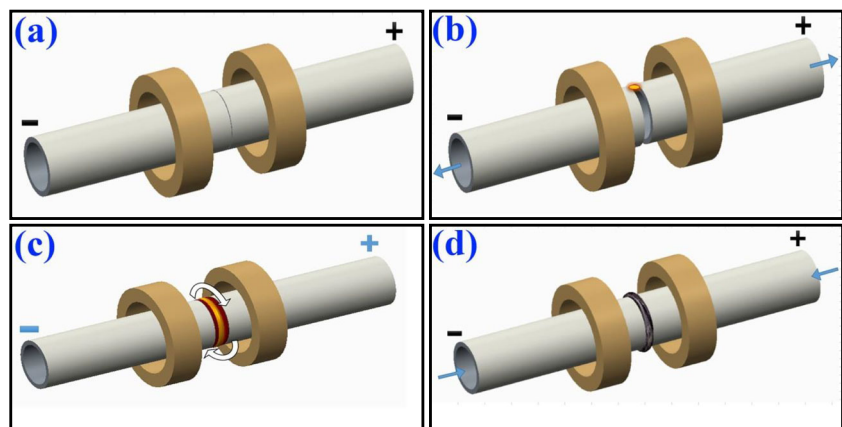
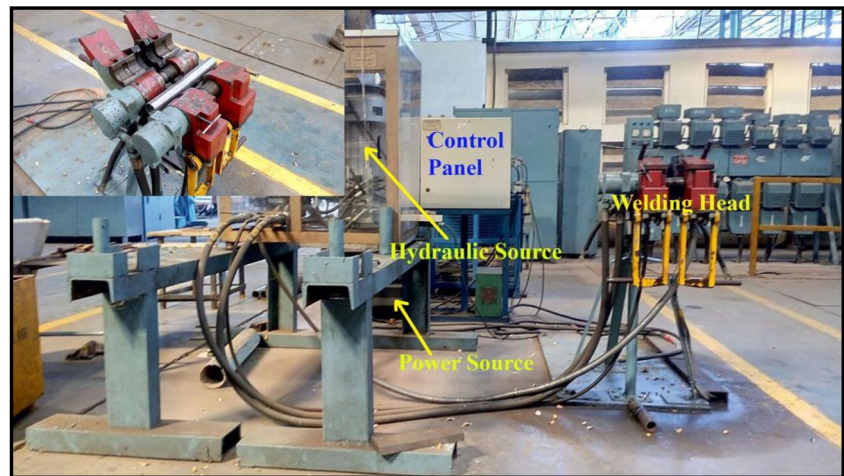


**Fig. 2** Experimental facility for MIAB welding



$$H = \frac{V(I_2 T_3 + I_3 T_4)}{A} \quad (2)$$

where  $H$  is heat input ( $\text{J}/\text{mm}^2$ ),  $V$  is arc voltage (V),  $I_2$  is arc rotation current (amps),  $T_3$  is arc rotation time (s),  $I_3$  is upset current (amps),  $T_4$  is upset time (s), and  $A$  is annular area ( $\text{mm}^2$ ).

## 2.5 Performing tensile testing

Wire electric discharge machining (WEDM) was used to prepare samples from the welded tubes for tensile testing. The gauge length and the gauge width were respectively 40 mm and 7 mm. The flash was carefully removed and the surface was slightly polished to avoid notch effect. They were pulled using a computerized tensile testing facility (INSTRON 1195) at a cross head

**Table 4** Design matrix with its experimental results

Trial run	Welding parameters			Heat input ( $\text{J}/\text{mm}^2$ )	UTS (MPa)	Joint efficiency (%)
	$A$	$U$	$T$			
MW01	-1	-1	-1	454	344	70.20
MW02	-1	-1	1	726	348	71.02
MW03	-1	1	-1	465	321	65.51
MW04	-1	1	1	738	329	67.14
MW05	1	-1	-1	497	359	73.27
MW06	1	-1	1	798	367	74.90
MW07	1	1	-1	508	331	67.55
MW08	1	1	1	809	355	72.45
MW09	-1.682	0	0	576	327	66.73
MW10	1.682	0	0	673	343	70.00
MW11	0	-1.682	0	615	351	71.63
MW12	0	1.682	0	634	337	68.78
MW13	0	0	-1.682	386	348	71.02
MW14	0	0	1.682	863	362	73.88
MW15	0	0	0	624	497	101.43
MW16	0	0	0	624	486	99.18
MW17	0	0	0	624	497	101.43
MW18	0	0	0	624	495	101.02
MW19	0	0	0	624	488	99.59
MW20	0	0	0	624	498	101.63

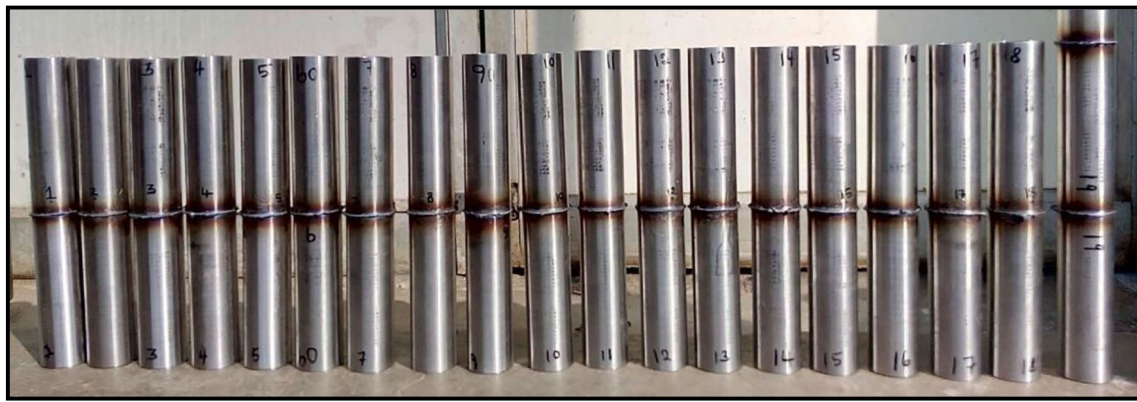


Fig. 3 Batch of MIAB welded AISI 409 FSS tubes

speed of 1 mm/min until fracture. The values of ultimate tensile strength (UTS) along with joint efficiency are recorded in Table 4. The tensile strength of the purchased 409 FSS is 490 MPa. A batch of fractured tensile specimens at various locations is shown in Fig. 4. Fractured surfaces of chosen specimens were observed by FESEM (CARL ZEISS SIGMA HV).

### 2.6 Procedure to develop an empirical relationship

The response function which represents the UTS of the welded joints as a function of arc rotation current (A), upset current (U), and arc rotation time (T) is stated by

$$R = f(A, U, T) \tag{3}$$

The second-order polynomial regression equation representing the response “Y” for *k* factors is written as

$$Y = b_0 + \sum_{i=1}^k b_i x_i + \sum_{i=1}^k b_{ij} x_i x_j \tag{4}$$

The chosen polynomial for three factors is expressed for all the responses as follows:

$$R = b_0 + b_1 I + b_2 F + b_3 W + b_{11} I^2 + b_{22} F^2 + b_{33} W^2 + b_{12} IF + b_{13} IW + b_{23} FW \tag{5}$$

where *b*<sub>0</sub> is the average of responses and *b*<sub>1</sub>, *b*<sub>2</sub>, *b*<sub>3</sub>, *b*<sub>11</sub>, *b*<sub>22</sub>, *b*<sub>33</sub>, *b*<sub>12</sub>, *b*<sub>13</sub>, and *b*<sub>23</sub> are the response coefficients that depend on respective main and interaction effects of parameters. The coefficients of each term were calculated using statistical software (SYSTAT 12). The empirical relationship was developed after the values of coefficients were found. The coefficients were tested for their significance level at 95% confidence level. Student *t*-test was used to eliminate insignificant coefficients and the final model was arrived which included only significant coefficients as given below.

$$UTS(\text{MPa}) = 493.224 + 7.095A - 7.728U + 4.946T - 54.216A^2 - 51.035U^2 - 47.147T^2 \tag{6}$$

### 2.7 Checking the adequacy of the empirical relationship

The empirical relationship was subjected to a statistical evaluation and the results are furnished in Table 5. The empirical relationship was found to have large “*R*-square” value and smaller standard error (SE). This observation assures that the empirical relationship can be effectively applied for predicting the response. Analysis of variance (ANOVA) of the empirical relationship is given in Table 5. *F*-ratio of the developed relationship (309.032) is much larger compared to the tabulated *F*-ratio (2.92) at 95% confidence level. Furthermore, the

Fig. 4 Batch of tensile tested specimens fractured at **a** weld interface and **b** base metal

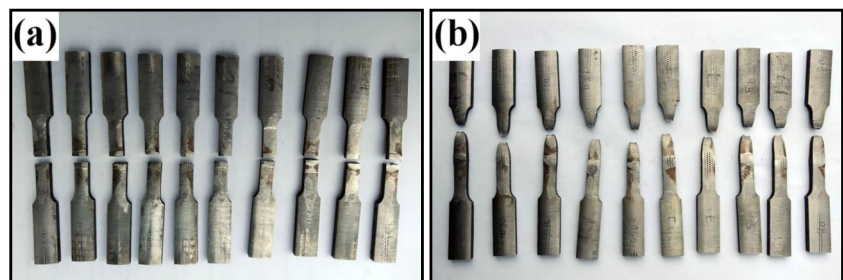


**Table 5** Statistical and ANOVA results of the developed empirical relationships

Dependent variable	$UTS$	
$N$	20	
Multiple $R$	0.997	
Squared multiple $R$	0.993	
Adjusted squared multiple $R$	0.990	
Standard error of estimate	7.171	
<b>Regression coefficients <math>B = (X'X)^{-1}X'Y</math></b>		
<b>Effect</b>	<b>Coefficient</b>	<b>Standard error</b>
Constant	493.224	2.925
$A$	7.095	1.940
$U$	-7.728	1.940
$T$	4.946	1.940
$A * A$	-54.216	1.889
$U * U$	-51.035	1.889
$T * T$	-47.147	1.889
<b>Analysis of variance</b>		
<b>Source</b>	<b>Type III SS</b>	<b>df</b>
Regression	95,338.120	6
Residual	668.430	13
	<b>Mean squares</b>	<b>F-ratio</b>
	15,889.687	309.032
	51.418	
	<b>Tolerance</b>	<b><math>t</math></b>
	1.000	168.650
	1.000	3.657
	1.000	-3.983
	1.000	2.549
	0.982	-28.708
	0.982	-27.024
	0.982	-24.965
		<b><math>p</math> value</b>
		0.000
		0.003
		0.002
		0.024
		0.000
		0.000
		0.000

scattering range of predicted and actual values was observed to be closer to the diagonal of the scatter plot in Fig. 5 which is a validation for adequacy of the relationship.

## 2.8 Characterization of joints

Samples for microstructural study were carefully ground and polished using a semiautomatic polishing machine. Alumina and diamond suspension was used in the final stage to obtain a flat surface resembling a mirror. Etching was performed using a solution of 5ml HNO<sub>3</sub>, 10ml glycerol, and 15 ml HCl to reveal the grainy structure. Macrographs of the joint regions were recorded using a stereomicroscope (OLYMPUS SZX16). Optical micrographs were captured using a conventional microscope (OLYMPUS BX51 M). EBSD was performed in an FEI Quanta FEG SEM equipped with TSL-OIM software. Microhardness indentations (500 g load for 15 s) were made across the fusion zone at the center of the thickness.

## 3 Results and discussion

The effect of each chosen process parameter on the joint strength was estimated using the developed empirical relationship. The coded values of each parameter were substituted to obtain the predicted value. Each parameter coded value was substituted five times (−1.682, −1, 0, 1, and 1.682) while keeping the rest of the parameters at central points (coded value of 0) to obtain the predicted trend. The predicted trends are expounded in this section and related to the observed changes in microstructural characterization.

### 3.1 Effect of arc rotation current

Arc rotation current is the current flowing across the faying surfaces during the stable arc rotation period. This is responsible for heating the surfaces to molten state and prepares the joint region to enable hot forging [13]. The influence of arc rotation current can be obtained by microstructural characterization of trail welds of MW09 (−1.682,0,0), MW15 (0,0,0), and MW10 (1.682,0,0) which are taken as typical samples to represent the effect. Hence, the role of arc rotation current on the macrographs can be assessed from Fig. 6a, g, and b. It is obvious that the size of TMAZ increases as the arc rotation current is increased. The increase in arc rotation current supplies more heat energy for joining. According to Kachinskiy et al. [13], the welding arc has an axial component and the magnetic field has a radial component. The interaction of the radial component of the magnetic field induction with the axial component of the welding current creates a driving arc force in the gap between the pipes. Increased arc current amplifies the magnetic force in the gap which further impels the rotating arc [22]. The rate of heating is eventually increased at

higher current (Table 4). The addition of heat preheats more and more material adjacent to the joint region. Therefore, the size of TMAZ is enlarged. A careful observation of Fig. 6a reveals that the preheating and the axial shortening are low at 458 amps. The joint is barely forged and the forging is insufficient. The heat energy available is insufficient for making a sound joint. Vignesh et al. [21] observed the emergence of cracks and unbonded regions at the lowest current of their experimental conditions. On the other hand, the joint prepared using 542 amps ejected more molten metal (Fig. 6b) which is inferred from the bigger size of the flash. The joint interface shows an array of dark spots which may represent voids or trapped oxide particles. Vendan et al. [17] reported a complete melting of the edges at the higher current limit of their experimentation which resulted in chaotic expulsion of material during forging. The joint prepared using 500 amps shows (Fig. 6g) properly consolidated structure, continuous interface, and optimum upset.

The effect of arc rotation current on the grain structure of the weld interface can be understood from Fig. 7a, g, and b. The size of the grain structure becomes bigger as the arc rotation current is increased. The average grain size was measured to be 2.82 μm at 458 amps and 11.3 μm at 542 amps. The forging force was not varied during welding but the grain structure evolution was not the same. This is due to the size of the grains during the heating period just before upsetting. The increase in arc rotation current increased the heat energy which increased the size of the preheated grains next to weld interface. Increasing heat energy slows down the cooling rate. Slower cooling rate provides extra time to expose the grains to heating. The upsetting is not done in an enclosure. The joint region is not constrained from expansion. This condition favors the grain growth. Hence, an increase in arc rotating current causes an increase in grain size.

The predicted effect of arc rotation current on the joint strength is plotted in Fig. 8. The predicted UTS was

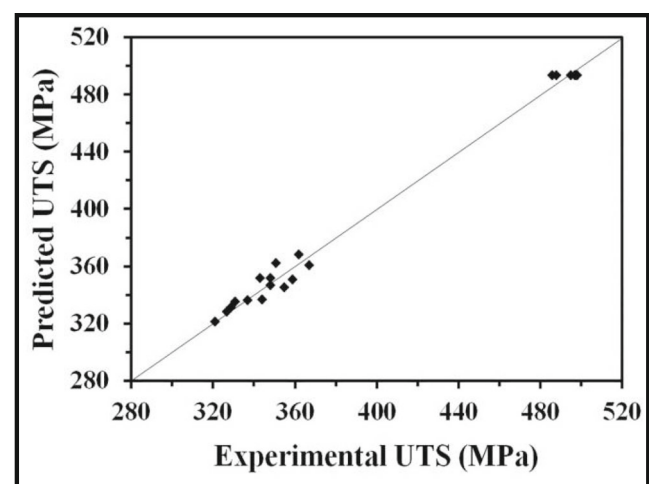


Fig. 5 Scatter diagram for the developed empirical relationship

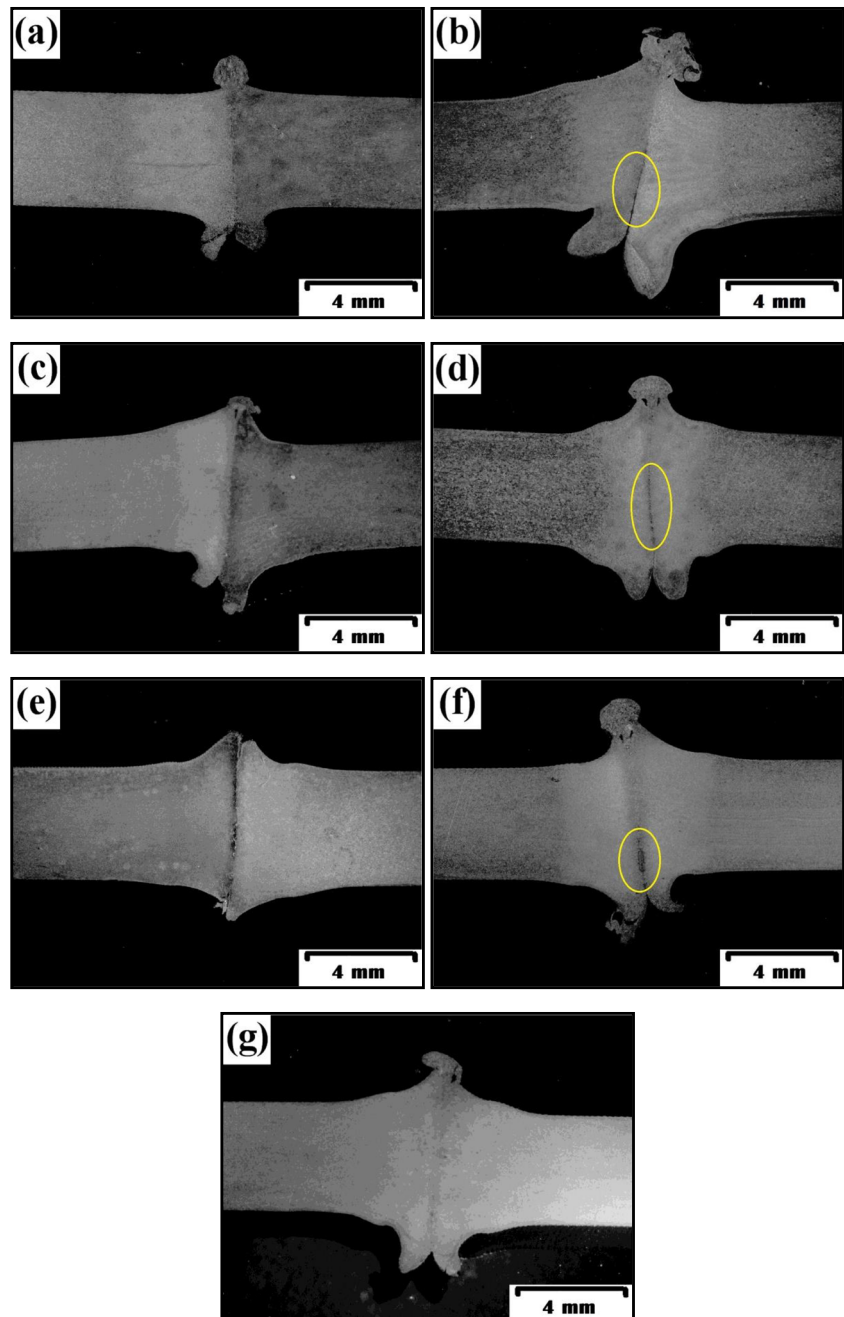
328 MPa at 458 amps and increases to 493 MPa at 500 amps. UTS drops with further increase in arc rotation current and is predicted to be 352 MPa at 542 amps. Improper forging is the cause of early failure at 458 amps which failed at the interface. The consolidated structure is inefficient to withstand the tensile load and ripped apart in a short duration. The fracture surface (Fig. 9a) is extremely flat and does not show the formation of dimple structure. There is an evidence for accelerated failure. The presence of voids reduced the supporting area to resist the tensile load and resulted premature failure during tensile test at the weld interface. The fracture surface (Fig. 9b) shows a large size crack which is caused due to progression of

fracture through voids at the interface. Stress concentration occurs due to voids which initiates failure at an early stage and prevents to resist more load. The joint strength is high at 500 amps due to properly forged structure which allowed to resist more tensile load and did not fail early. The joint fractured away from the interface at the base metal. The fracture surface shows (Fig. 9g) a network of well-developed dimples.

### 3.2 Effect of upset current

Upset current is the current supplied during the upsetting period of the MIAB welding cycle. The purpose of the upsetting

**Fig. 6** Optical macrographs of the MIAB weld joints of trial runs; **a** MW09, **b** MW10, **c** MW11, **d** MW12, **e** MW13, **f** MW14, and **g** MW15





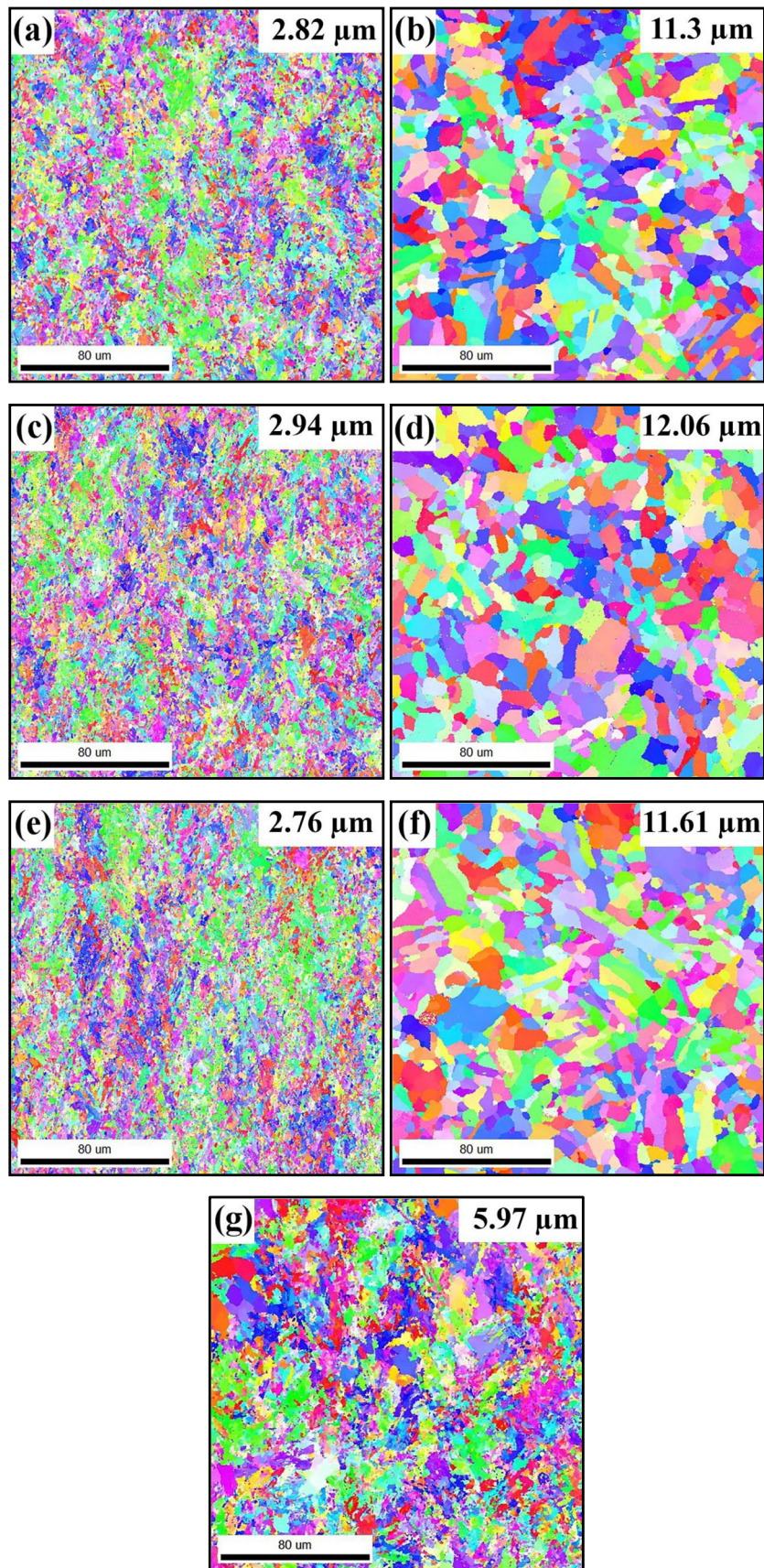


**Fig. 7** EBSD (IPF + grain boundary) maps of the weld interface of MIAB weld joints of trial runs; **a** MW09, **b** MW10, **c** MW11, **d** MW12, **e** MW13, **f** MW14, and **g** MW15

current is to obtain a uniform melt on the surface of the pipes to be welded. Intensive renewal of the melt at the butt surface leads to the formation of a welded joint during the upsetting process. It further provides a cleaning action through proper expulsion of impurities [33]. The effect of upset current can be explained by the microstructural characterization of trial welds of MW11 (0,−1.682, 0), MW15 (0,0,0), and MW12 (0,1.682, 0) as representative samples. Hence, the effect of upset current on the macrographs can be seen from Fig. 6c, g, and d. It is discernable from the macrographs that the size of TMAZ becomes larger with an increase in upset current. The variation in upset current causes a variation in heat input as documented in Table 4. More heat energy is supplied to the joint region as the quantity of upset current increases [22]. This overheats the material which is already preheated during arc rotation period. The net effect is an increase in the size of TMAZ at the end of upsetting stage. The macrograph at upset current of 732 amps shows (Fig. 6c) that the deformation during upsetting is small and the forging is not achieved completely. The joint hangs on the interface without intense penetration of deformed material because of lower heating. Vendan et al. [17] observed little flash and inadequate penetration at lower upset current and concluded that the upset current governed the forging stage of the MIAB welding cycle. The macrograph at upper limit of 1068 amps shows (Fig. 6d) broadened TMAZ and the flash size is bigger. There are possibilities of oxide particles and void formation appearing as dark spots at the weld interface. The higher limit of upset current led to excessive heating which increased the thickness of molten metal. The macrograph of the joint at 900 amps (Fig. 6g) appears to be optimum without excessive flash or lack of consolidation. Sivasankari et al. [33] stressed that the increase in upset current purged the contaminants from the joint region and promoted the quality of the joints.

The impact of upset current on the grain structure of the weld interface can be comprehended from Fig. 7c, g, and d. The increase in upset current caused an enlargement of grain structure. The average grain size was estimated to be 2.76  $\mu\text{m}$  at 732 amps and 11.16  $\mu\text{m}$  at 1068 amps. The preheating cycle (arc rotation current, arc rotation duration) was the same for these joints. Therefore, the preheated grain size before upsetting was the same. Both current and pressure are applied during upsetting. The magnitude of the latter factor was kept constant. Upsetting current supplies more heat attempting to increase the grain size. The upset pressure deforms the material attempting to reduce the grain size. The trend observed in Fig. 7 shows an increasing curve. Since a constant upset pressure was applied, the increase in upset current increased the size of grains due to higher heat input. The effect of heating overrides the effect of deformation to enlarge the grain structure. The effect can be compared to the effect of annealing a fine-grained material. The fine grains tend to grow up during annealing. Similarly, the upset current

disrupts the fine grain structure and supplies additional heat energy to grow up.

The predicted effect of upset current on the joint strength is presented in Fig. 10. The predicted UTS was 362 MPa at 732 amps and increases to 336 MPa at 500 amps. UTS reduces with further increase in upset current and is predicted to be 352 MPa at 1068 amps. Insufficient forging is the cause of poor joint strength at upset current of 732 amps. The joint failed at the weld interface quickly without reaching the ultimate tensile load. The fracture surface (Fig. 9c) shows no evidence of necking due to flat nature of the surface. Failure occurred in the early stage without the development of dimples. Similarly, the joint at upset current of 732 amps encountered premature failure during tensile testing. The voids at the interface reduced the effective area to withstand the tensile load. They accumulate unnecessary stress at the interface and act to initiate failure. The fracture surface is observed (Fig. 9d) to have failure marks of voids in the form of dark pits on it. The joint prepared using upset current of 900 amps provided highest joint strength failing at a distance from the weld interface on the base metal (Fig. 4b). The consolidated forged structure is optimum to arrest the failure of the interface.

### 3.3 Effect of arc rotation time

Arc rotation time (or arc duration) is the duration that the arc rotates along the annular space. This is the heating period of the welding cycle to prepare the joint region for upsetting [17]. This parameter can be compared to friction time in friction welding process [9]. The role of arc duration can be inferred through microstructural characterization of trail welds of MW13 (0,0,−1.682), MW15 (0,0,0), and MW14 (0,0,1.682) which typically correspond the effect. Therefore, the effect of arc duration on the macrographs can be understood from Fig. 6e, g, and f. The macrographs in this order show clearly that the size of TMAZ increases with an increase in arc duration.

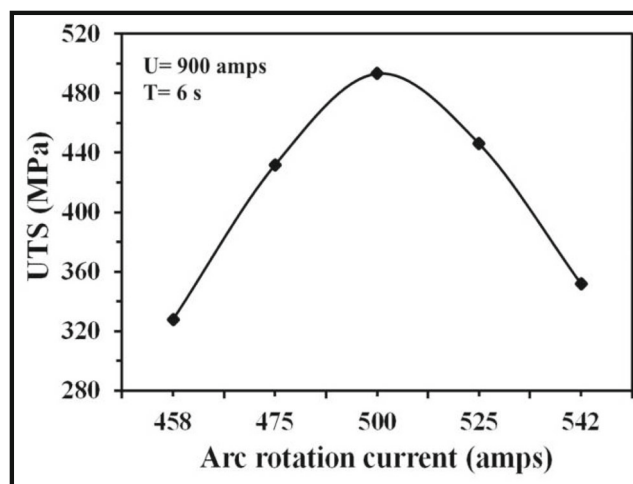
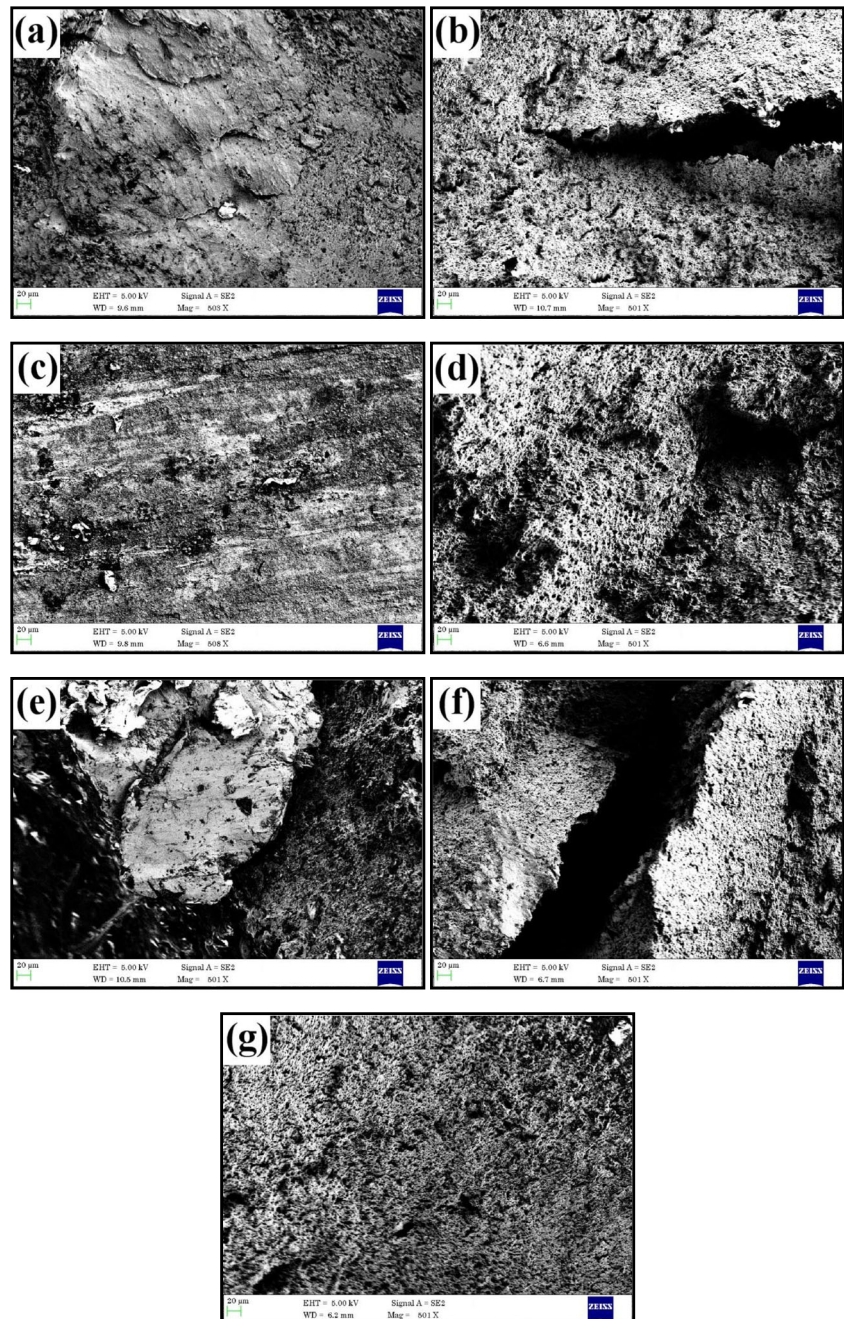


Fig. 8 Variation of UTS as a function of arc rotation current

The arc duration determines the available quantity of heat energy from the rotating arc as calculated in Table 4. The increase in arc duration results in the supply of more heat energy to the joint region [21]. The rate of heating, i.e., the slope of arc duration and the heat energy is increased sharply. Increased heat energy is conducted in the traverse direction for preheating more adjacent region. This is the cause for the enlargement of TMAZ region. The macrograph (Fig. 6e) at arc duration of 4 s shows that the upsetting is insufficient and the axial shortening is low. This observation suggests that the

welding condition resulted in poorly forged structure. The heat input at 4 s did not provide sufficient preheating for proper forging. The macrograph at 8 s (Fig. 6f) shows a larger size flash and ejected molten metal. The interface is crumbled and not perfectly straight. There are dark spots at the interface that represent the locations of voids and oxide particles. The increase in arc rotation time allows more volume of material to be heated because of increase heat transfer. Conversely, the macrograph (Fig. 6g) at 6 s shows a perfectly aligned interface without any kind of inclusions. The size of flash and the axial

**Fig. 9** SEM micrographs of failed tensile specimens of the MIAB weld joints of trial runs; **a** MW09, **b** MW10, **c** MW11, **d** MW12, **e** MW13, **f** MW14, and **g** MW15



shortening appear to be optimum. Vendan et al. [17] observed that arc rotating time is crucial to obtain sound joints because it contributes for a longer duration of the weld cycle.

The influence of arc duration on the grain size of the weld interface can be assessed from Fig. 7e, g, and f. The grain size became larger with an increase in arc duration as expected. The average grain size was calculated to be 2.94  $\mu\text{m}$  at 4 s and 12.06  $\mu\text{m}$  at 8 s. The forging conditions (upset pressure, upset current, and upset time) were identical for those joints. Same degree of deformation did not yield same degree of grain refinement. The variation of grain size is owing to variation in grain size at the end of the heating period. Increased arc duration contributed to incremental supply of additional heat energy. Increase in preheating caused grain coarsening in adjacent regions to the weld interface. Higher heat input reduces the rate of cooling. Hence, the grain refinement did not occur to the same level. The drop in cooling rate subjects the grains to further heating. More the grain size during heating period more will be the grain size after upsetting because the forged material is not constrained to expand.

Fig. 11 shows the predicted effect of arc duration on the joint strength. The predicted UTS was 352 MPa at 4 s and increases to 493 MPa at 6 s. UTS drops with further increase in arc rotation current and is predicted to be 368 MPa at 8 s. The joint fabricated at 4 s did not have sufficient upset to make a proper forged structure. This kind of joint does not endure more loading and separates into two pieces in a shorter duration at the weld interface. The fracture surface (Fig.9e) does not show signs for the evolution and the growth of dimples. The failure progressed at rapid pace to fracture the specimen. The joint made at 8 s also succumbed to failure at an early stage. The existence of voids did not allow to accept higher loading. The fracture surface (Fig.9f) shows partially grown up dimple structure. The dark empty spaces represent the spots of voids and initiation of failure. Voids lead to undesirable stress contraction at the juncture of discontinuities at the weld interface. A higher joint strength at 6 s is attributed to excellent forged structure which received the highest load until the ultimate point crossed. The weld interface remained intact (Fig. 4b) and failure took place at the interface. Failure occurred by the coalescence of completely grown up dimples.

### 3.4 General discussion

The nature of the joint interface presents a crucial effect on the joint strength. An interface free from contamination and voids as well as fully forged structure is required to achieve higher joint strength. A slight variation in the process parameter and their improper choice may have an adverse effect on the process [17]. Extreme limits of the chosen parameter range provided improper forging and voids at the interface. Figure 12 presents optical macrographs of some of the joints prepared between the limits. Micron-sized voids and oxide particles are

found in some joints (Fig. 12a and b). They create spots of poor adhesion at the interface and act as failure initiating sites during the tensile test. The interface is clear and straight in some joints (Fig. 12c and d). There is no external evidence for the presence of voids. However, there is a possibility for internal oxide particle and pores. This is the cause for the variation of tensile strength between limits as plotted in Figs. 8, 10, and 11. Since the welding cycle is shorter in MIAB welding, a shielding gas is seldom used. Iordachescu et al. [16] believed that nitrogen or other reducing or inert gases could enhance the weld quality. Vendan et al. [19] found small sized pores at TMAZ and attributed the pore formation because of the interaction with atmospheric gas molecules. They suggested that the use of shielding gas could possibly eliminate pores.

Figure 13 records various kinds of interfaces observed in the joints. Large size of discontinuous voids and small size of continuous voids are respectively observed in Fig. 13a and b. Void acts as a discontinuity across the joint region and magnifies the applied stress as a result of notch effect. The fracture propagates easily through continuous voids. A higher limit of the heat input is observed to form voids. A layer of excessive molten metal appears which causes a momentary instability during upsetting. The interface is not perfectly straight and adhering which leaves voids. The interface is slightly darker and has black spots in Fig. 13c. This condition represents the presence of oxide particle which does not endure the tensile load. The brittle oxide particle fractures easily leaving the joint weaker. The interface in Fig. 13d has a remnant of a solidified material of few microns thick. This is a common feature in MIAB welded joints as reported by earlier investigators [16, 19, 20]. Sivasankari et al. [33] called this kind of layered region as a light-banded zone. They reported that the magnitude of the upset current influences the formation. Higher upset current completely eliminated this layer. This layer does not impact the joint strength adversely. However, a thick

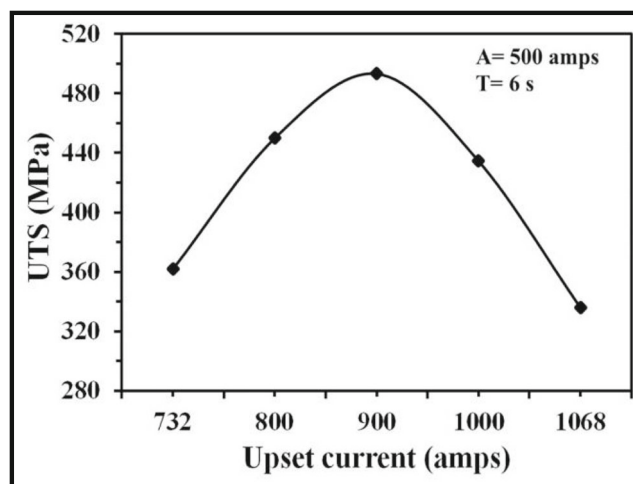


Fig. 10 Variation of UTS as a function of upset current

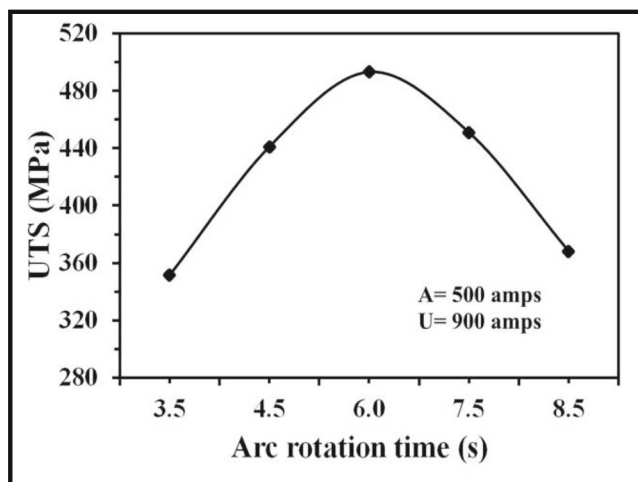


Fig. 11 Variation of UTS as a function of arc rotation time

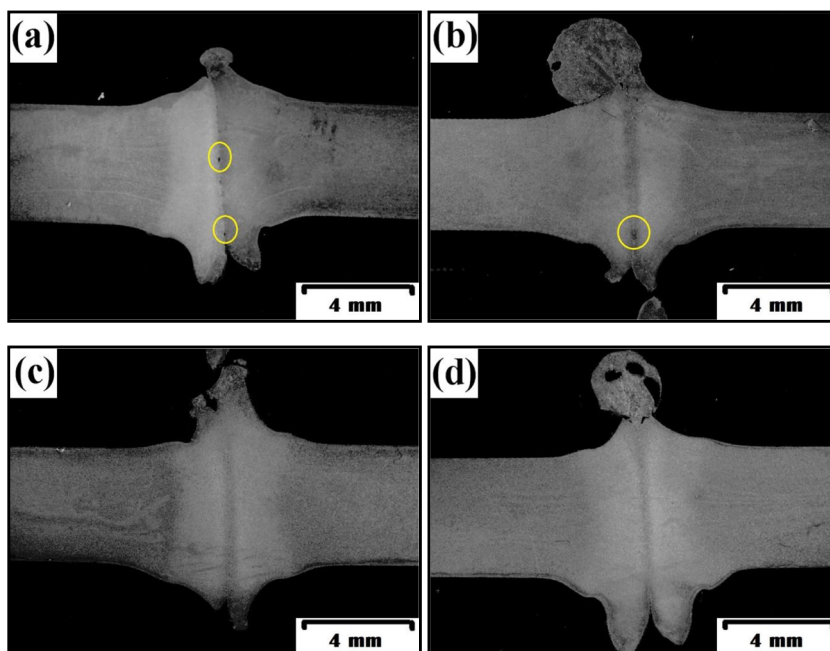
solidified layer may reduce the load-bearing capacity to some extent. The interface is hard to find at the middle of the micrograph in Fig. 13e. The molten metal was completely expelled during upsetting leaving no traces of solidified layer. The preheated edges were properly forged similar to a typical solid-state joint. This kind of interface is highly preferred because it provides higher joint strength closer to the strength of the base metal.

Figure 14 reveals optical micrographs of the joint region from unaffected base metal to weld interface. It is obvious that the grain structure is a function of the distance from the weld interface. The grain size continuously reduces towards the weld interface. The amount of deformation and the quantity of heat prevailing would reduce as the distance from the weld interface increases. Weld interface is subjected to intense

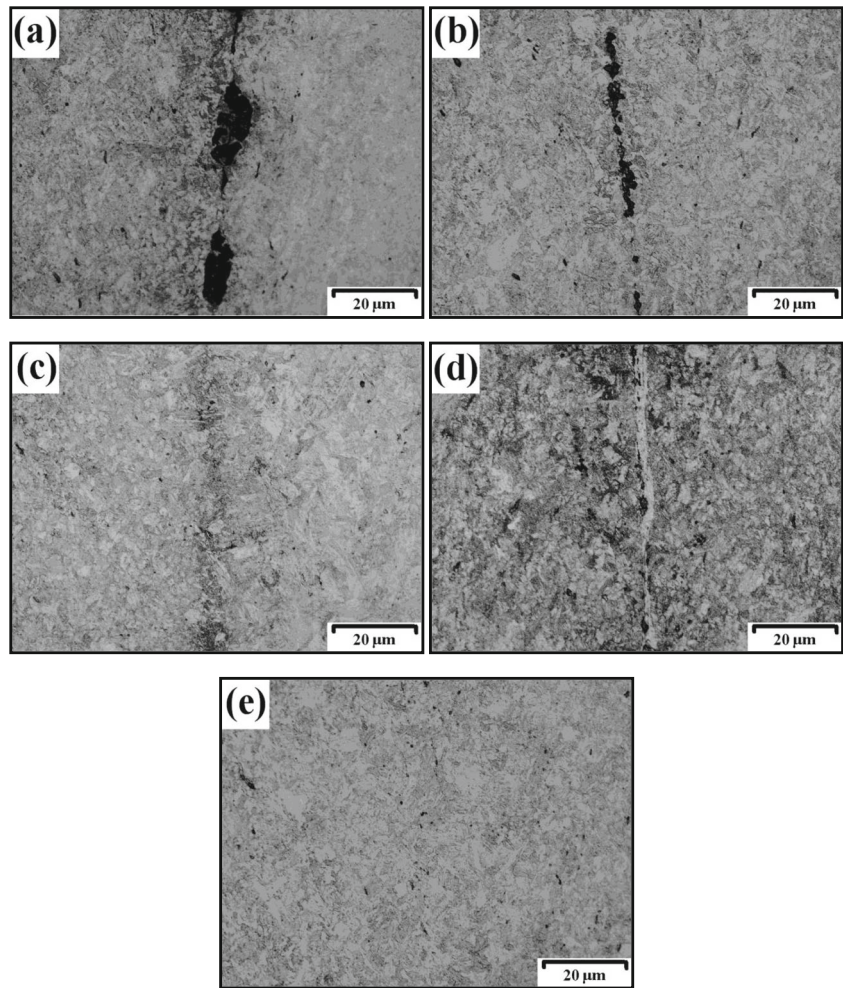
deformation which drastically refines the grain structure. On the other hand, the edges of TMAZ receive little deformation which is inadequate to make a huge refinement. Nevertheless, the grain size of TMAZ at any given location did not exceed to that of base metal. Similar observation was recorded by Iordachescu et al. [16]. They stated that different regions are subjected to different intensities of the thermal cycle. The peak temperature and the cooling rate vary while moving away from the joint region. MIAB welding did not produce a coarser grain region commonly known as HAZ in typical fusion-welded joints. The grain growth during arc rotation time is offset by the effect of upsetting. The previous grain structure is masked by the deformation grain structure. Furthermore, Vignesh et al. [21] stated that the welded tubes can be handled without using safety gloves or any devices to hold. They stated that the cooling rate is much faster than the welding cycle does not cause accumulation of heat on the tube. The possibility for grain coarsening is remote.

Figure 15 presents the hardness profiles of some of the joints. Similar pattern was found in all the joints. The hardness of the TMAZ is almost 300 HV higher to that of base metal AISI 409 FSS. MIAB welding provided enormous strengthening of the joint region. Ferrite phase did not transform into martensite or other kinds of bainite structure as seen in Fig. 13. The high amount of Cr element bars the transformation of ferrite into austenite during a heating cycle. Therefore, the strengthening did not occur due to the emergence of hard phases during the thermal cycle. Fine grain structure and the deformation of material imparted strengthening. Deformation generates huge amount of strain fields within TMAZ. Strengthening of the weld zone is advantageous to obtain higher joint strength and push the fracture location towards

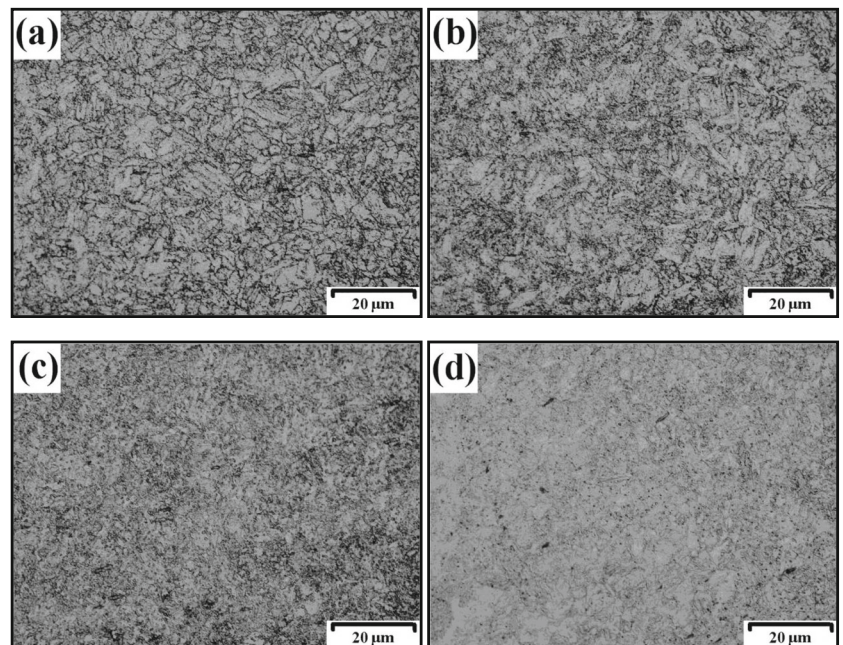
Fig. 12 Optical macrographs of the MIAB weld joints of trial runs; a MW03, b MW04, c MW06, and d MW08



**Fig. 13** Optical micrographs of the MIAB weld interface showing; **a** large voids (MW14), **b** continuous voids (MW12), **c** oxide particles (MW06), **d** solidified layer (MW08), and **e** clear interface (MW15)



**Fig. 14** Optical micrographs of MIAB welded joint M18 showing; **a** base metal; **b** edge of TMAZ, **c** middle of TMAZ, and **d** near weld interface



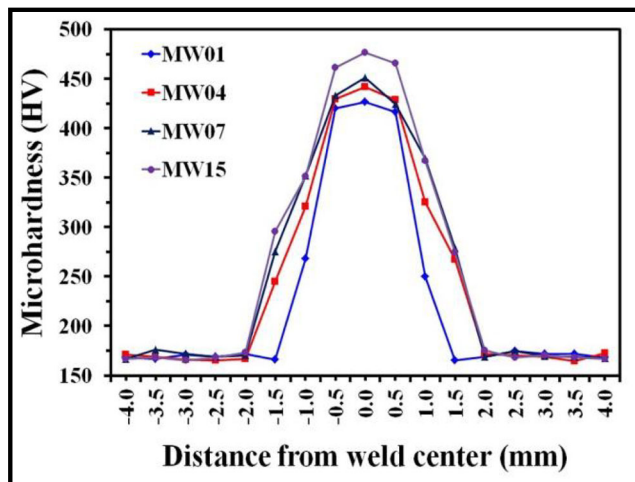


Fig. 15 Microhardness distribution across MIAB welded joints

base metal. MIAB welding provided similar kind of strengthening on several materials [18, 20]. Iordachescu et al. [16] observed a hardness of 260 HV at the midpoint of TMAZ which is 80 HV higher than their base metal ST37 steel. Vignesh et al. [21] reported a hardness of 620 HV at the middle of TMAZ which is 340 HV higher compared to their base metal T11 pipe steel. Although all the joints exhibited strengthening of TMAZ, many joints failed at the weld interface. The nature of the interface is an important aspect of MIAB welding as mentioned previously.

## 4 Conclusions

MIAB welding was used efficiently to join 4-mm thick AISI 409 FSS tubes. DOE approach was used for experimentation to develop an empirical expression for the prediction of joint strength under various welding conditions. The conclusions from the present research are summarized below.

- Lower limits of process parameters showed improper forging due to lack of preheating and consolidation. Higher limits of process parameters caused a momentary instability during upsetting and produced voids as well as oxide particles at the weld interface. The joint failed prematurely because of these issues. The variation in joint strength between the limits of process parameters was attributed to spots of low adhesion due to micron size voids and oxide particles.
- The weld region was fully composed of deformed structure which was affected by the heat energy of the arc and the compressive force of the upsetting stage. Hence, the weld region was called as TMAZ.
- The increase in chosen process parameters, namely, arc rotation current, upset current, and arc rotation time caused an enlargement of TMAZ region and increased

the grain structure of the weld interface. This result is due to an increase in heat energy supplied to the joint interface for preheating and during upsetting.

- The grain structure of the TMAZ was dependent on the distance from the weld interface. The increase in distance from the weld interface reduced the available heat and the deformation. The size of the grains in TMAZ was lower to that of base metal. Ferritic phase did not experience any phase transformation due to the thermal cycle of MIAB welding.
- TMAZ exhibited significant strengthening due to grain refinement and deformed structure. Nevertheless, obtaining a clearly forged interface without any contamination was necessary to obtain higher joint strength and move the fracture location towards base metal. Highest joint strength matching to the base metal was obtained under a welding condition of  $A = 500$  amps,  $U = 900$  amps, and  $T = 6$  s.

**Acknowledgements** Authors are grateful to Welding Research Institute at Bharat Heavy Electricals Limited, Tiruchirappalli, Speed Spark EDM at Coimbatore, Microscopy lab at the University of Johannesburg, OIM and Texture Lab at Indian Institute of Technology Bombay, and The South India Textile Research Association for providing the facilities to carry out this investigation.

**Author contribution** T. Muthu Krishnan: conceptualization, investigation, project administration, data curation, proofreading. I. Dinaharan: conceptualization, investigation, data curation, writing—original draft, supervision. R. Palanivel: investigation, data curation, proofreading. C. Balamurugan: data curation, proofreading.

**Funding** No funding was received to execute this project from any funding body. All the expenses were borne by the authors.

**Data availability** The raw/processed data required to reproduce these findings cannot be shared at this time due to legal or ethical reasons. The raw/processed data required to reproduce these findings cannot be shared at this time due to technical or time limitations.

## Declarations

**Ethical approval** Not applicable.

**Consent to participate** Not applicable.

**Consent to publish** Not applicable.

**Competing interests** The authors declare no competing interests.

## References

1. Van Zwieten ACTM, Bulloch JH (1993) Some considerations on the toughness properties of ferritic stainless steels—a brief review. *Int J Press Vessel Pip* 56:1–31

2. Lo KH, Shek CH, Lai JKL (2009) Recent developments in stainless steels. *Mater Sci Eng R* 65:39–104
3. Wei LL, Chen LQ, Ma MY, Liu HL, Misra RDK (2018) Oxidation behavior of ferritic stainless steels in simulated automotive exhaust gas containing 5 vol.% water vapor. *Mater Chem Phys* 205:508–517
4. Ma XG, Zhao JW, Du W, Jiang ZY (2020) Effects of cold rolling and annealing on the ridging behaviour of ferritic stainless steel. *Int J Adv Manuf Technol* 107:4823–4836
5. Mohandas T, Madhusudhan Reddy G, Naveed M (1999) A comparative evaluation of gas tungsten and shielded metal arc welds of a “ferritic” stainless steel. *J Mater Process Technol* 94:133–140
6. Amuda MOH, Mridha S (2012) Comparative evaluation of grain refinement in AISI 430 FSS welds by elemental metal powder addition and cryogenic cooling. *Mater Des* 35:609–618
7. Taban E, Deleu E, Dhooge A, Kaluc E (2007) Gas metal arc welding of modified X2CrNi12 ferritic stainless steel. *Kovove Material* 45:67–74
8. Vidyarthi RS, Dwivedi DK, Vasudevan M (2017) Influence of M-TIG and A-TIG welding process on microstructure and mechanical behavior of 409 ferritic stainless steel. *J Mater Eng Perform* 26:1391–1403
9. Uday MB, Fauzi MNA, Zuhailawati H, Ismail AB (2010) Advances in friction welding process: a review. *Sci Technol Weld Join* 15:534–558
10. Kim KH, Bang HS, Bang HS, Kaplan AFH (2017) Joint properties of ultra thin 430M2 ferritic stainless steel sheets by friction stir welding using pinless tool. *J Mater Process Technol* 243:381–386
11. Taneko A, Arakida F, Takagi K (1987) Analysis of arc rotation velocity in magnetically impelled arc butt welding. *Weld Int* 3:247–253
12. Mori S, Yasuda K (1990) Magnetically impelled arc butt welding of aluminium pipes. *Transact Japan Weld Soc* 21:3–10
13. Kachinskiy VS, Krivenko VG, Ignatenko VY (2002) Magnetically impelled arc butt welding of hollow and solid parts. *Weld World* 46:49–56
14. Kim JW, Choi DH (2003) A study on the numerical analysis of magnetic flux density by a solenoid for magnetically impelled arc butt welding. *Proc Inst Mech Eng B J Eng Manuf* 217:1401–1407
15. Yapp D, Blackman SA (2004) Recent developments in high productivity pipeline welding. *J Braz Soc Mech Sci Eng* 26:89–97
16. Iordachescu D, Iordachescu M, Georgescuc B, Mirandad RM, Ruiz-Hervias J, Ocana JL (2010) Technological windows for MIAB welding of tubes featuring original longitudinal magnetization system with peripheral solenoids. *J Mater Process Technol* 210:951–960
17. Vendan SA, Manoharan S, Buvanashakaran G, Nagamani C (2011) Magnetically impelled arc butt welding of alloy steel tubes in boilers – establishment of parameter window. *Mechatronics* 21:30–37
18. Vendan SA, Mundla SR, Buvanashakaran G (2012) Feasibility of magnetically impelled arc butt (MIAB) welding of high-thickness tubes for pressure parts. *Mater Manuf Process* 27:573–579
19. Vendan SA, Manoharan S, Nagamani C (2012) MIAB welding of alloy steel tubes in pressure parts: metallurgical characterization and nondestructive testing. *J Manuf Process* 14:82–88
20. Sivasankari R, Balusamy V, Venkateswaran PR, Buvanashakaran G, Ganesh Kumar K (2015) Characterization of magnetically impelled arc butt welded T11 tubes for high pressure applications. *Defence Technol* 11:244–254
21. Vignesh S, Dinesh Babu P, Prasanna Venkatesh V, Martin Vinoth S, Marimuthu P (2017) Experimental investigations on magnetically impelled arc butt welded T91 steel tubes. *Trans Indian Inst Metals* 70:741–748
22. Panda BN, Vendan SA, Garg A (2017) Experimental- and numerical-based studies for magnetically impelled arc butt welding of T11 chromium alloy tubes. *Int J Adv Manuf Technol* 88:3499–3506
23. Balta B, Arıcı AA, Yılmaz M, Gümüş S, Yücel SC (2018) Microstructural and mechanical properties of friction and MIAB welded carbon steel tubes and forging bracket joints. *Mater Test* 60:273–282
24. Mosayebnezhad J, Sedighi M (2018) Numerical and experimental investigation of residual stresses in magnetically impelled arc butt welded joints in low alloy steels. *Int J Adv Manuf Technol* 96:4501–4515
25. Kustron P, Piwowarczyk T, Korzeniowski M, Sokołowski P, Bicz A (2020) The Detectability of welding defects in MIAB welded thin-walled tubular components by immersion ultrasonic technique. *J Nondestruct Eval* 39:42
26. Elangovan K, Balasubramanian V, Babu S (2009) Predicting tensile strength of friction stir welded AA6061 aluminium alloy joints by a mathematical model. *Mater Des* 30:188–193
27. Giridharan PK, Murugan N (2009) Optimization of pulsed GTA welding process parameters for the welding of AISI 304L stainless steel sheets. *Int J Adv Manuf Technol* 40:478–489
28. Manonmani K, Murugan N, Buvanashakaran G (2007) Effects of process parameters on the bead geometry of laser beam butt welded stainless steel sheets. *Int J Adv Manuf Technol* 32:1125–1133
29. Rajakumar S, Balasubramanian V (2016) Diffusion bonding of titanium and AA 7075 aluminum alloy dissimilar joints—process modeling and optimization using desirability approach. *Int J Adv Manuf Technol* 86:1095–1112
30. Kannan T, Murugan N (2006) Effect of flux cored arc welding process parameters on duplex stainless steel clad quality. *J Mater Process Technol* 176:230–239
31. Montgomery DG (2001) *Design and Analysis of Experiments*. Wiley, Hoboken
32. Box GEP, Hunter WH, Hunter JS (1978) *Statistics for Experiments*. Wiley, New York
33. Sivasankari R, Balusamy V, Buvanashakaran G (2014) Effect of upset current in magnetically impelled arc butt (MIAB) welding of carbon steel tubes. *Appl Mech Mater* 592-594:240–244

**Publisher's note** Springer Nature remains neutral with regard to jurisdictional claims in published maps and institutional affiliations.